LITHOS 456-457 (2023) 107317

Contents lists available at ScienceDirect

LITHOS

journal homepage: www.elsevier.com/locate/lithos

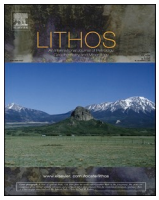

Microfabric evolution during metasomatism and deformation, exemplified by the nodular sillimanite gneisses (Bamble lithotectonic domain, South Norway)

A.K. Engvik [a,*], C.A. Trepmann [b], H. Austrheim [c]

[a] Geological Survey of Norway, Trondheim, Norway
[b] Department of Earth and Environmental Sciences, Ludwig-Maximilians-Universität München, Munich, Germany
[c] Department of Geosciences, University of Oslo, Oslo, Norway

ARTICLE INFO

Keywords:
Bamble
Metasomatism
Nodules
Reaction microfabrics
Sillimanite

ABSTRACT

Proterozoic foliated and nodular sillimanite gneisses from the Bamble lithotectonic domain, South Norway, are analysed to unravel their microfabric evolution with mineral reactions during metasomatism and associated deformation. The nodules form cm-scaled spherical to ellipsoidal sillimanite-quartz aggregates that locally grade into foliated sillimanite gneisses. Independent on their fabric, they record incomplete breakdown reactions of biotite and K-feldspar recorded by muscovite lamellae and associated Fe-oxide needles in biotite and by muscovite-quartz aggregates after K-feldspar. Muscovite is partly replaced by sillimanite. Based on immobile Al, the nodular gneiss forming reactions give excess K, Mg and H_2O that may leave the nodular gneiss to form a metasomatic agent and caused regional metasomatism (scapolitisation) in the surrounding rocks. Quartz in the foliated gneisses shows a pronounced shape but no marked crystallographic preferred orientation. There is no indication of major strain accumulation by quartz dislocation creep. Muscovite shows lobate phase boundaries to quartz, which is interpreted as reaction fabric, from the breakdown reactions of K-feldspar and biotite. The nodular and sillimanite gneisses formed during metasomatic mineral reactions, where major elements K, Mg and H_2O leave the rock and an Al-rich metasomatic restite remains. We suggest that the metasomatism involved a molar volume loss, where reactions forming muscovite, quartz and sillimanite occurred by incongruent dissolution-precipitation creep at low stresses forming the nodular and foliated gneisses. Our study demonstrates that metasomatism with chemical rock changes and mass transfer associated with incongruent dissolution-precipitation contributed to the observed reaction and deformation microfabric.

1. Introduction

Fluid infiltration play an active role in mineral reactions and growth (e.g., Engvik et al., 2005; Putnis and Austrheim, 2010; Wayte et al., 1989), important for modification of crust (e.g., Engvik et al., 2000; Fitz Gerald and Stünitz, 1993; Jamtveit et al., 2016). Fluids cause metasomatism by changing the chemical rock composition and mineralogy (e.g., Clark et al., 2005; Oliver et al., 2004) and act as catalysts during mineral transformations by dissolution of phases and precipitation of new ones (e.g., Putnis, 2002). The rocks interaction with fluids can cause albitization by Na-metasomatism (e.g., Ettner et al., 1993), scapolitisation by K-Mg-Cl metasomatism (Oliver et al., 1994), carbonitisation (Dahlgren et al., 1993) or K-metasomatism (Saunders and Tuach, 1988). The importance of metasomatism is illustrated by its large-scale influence as described from Precambrian crustal rocks worldwide (e.g., Ettner et al., 1993; Mark and Foster, 2000; Weisheit et al., 2013).

There is an ongoing discussion if deformation during fluid-induced metamorphism take place by dissolution-precipitation creep rather than by temperature-dependent dislocation creep (Putnis, 2021; Stöckhert et al., 1999; Wassmann et al., 2011; Wintsch and Yi, 2002). Metasomatic rocks resulting from metamorphism involving mass transfer display deformation structures like foliation, folding and shear zones (Hunter and Andronicos, 2013; McLelland et al., 2002b; Mukai et al., 2014). Deformation of rocks can increase the rates of mineral reactions and vice versa, e.g., during incongruent dissolution-precipitation creep, where increased solubility at sites of shortening

* Corresponding author.
E-mail addresses: ane.engvik@ngu.no (A.K. Engvik), claudia.trepmann@lmu.de (C.A. Trepmann), h.o.austrheim@geo.uio.no (H. Austrheim).

https://doi.org/10.1016/j.lithos.2023.107317
Received 23 April 2023; Received in revised form 7 August 2023; Accepted 11 August 2023
Available online 12 August 2023

enhances dissolution of an instable phase into the pore fluid and precipitation of a stable phase at sites of dilation (e.g., Putnis, 2021; Wassmann et al., 2011; Wassmann and Stöckhert, 2013; Wheeler, 1992; Wintsch et al., 2005; Wintsch and Yi, 2002). Also, fluids released in dehydration reactions may trigger brittle deformation by reducing the effective stresses ("dehydration embrittlement" e.g., Fagereng et al., 2018). And again vice versa, fluids introduced into former dry lithologies by enhancing the permeability via brittle deformation may trigger metamorphic reactions (e.g., Austrheim, 1987; Jamtveit et al., 2016). Fluid infiltration, metamorphic transformation and deformation may change a rock into a lithology with new mineralogy, chemistry and structure, and its origin can be difficult to interpret.

Sillimanite and nodular gneisses are reported worldwide, and sillimanite is often used as a key mineral during interpretation of metamorphic rock (e.g., Bernier et al., 1987; Nabelek, 1997; Spry et al., 2022; Vernon, 1979). The sillimanite is traditionally used to define metamorphic grade known as the high-temperature Al-silicate mineral in the Barrovian metamorphic concept (Barrow, 1912; Gillen, 1982). Its occurrence is usually in rocks of quartz and mica-rich schists and gneisses, locally occurring as the peculiar nodular gneisses with coarse white nuggets concentrating sillimanite in the gneiss (e.g., Munz et al., 1994; Vernon, 1979).

The origin of the sillimanite nodular gneisses has been disputed, and the understanding of their origin and formation of this special lithology affect modelling of geological history (e.g., Spry et al., 2022). While the presence of sillimanite has been taken to support a sedimentary rock origin (e.g., Spry et al., 2022), other studies have assigned their origin in a granitoid environment (McLelland et al., 2002a). From the Bamble lithotectonic domain of south Norway, the original descriptions by Brøgger (1934) explained the sillimanite nodular rocks as granitic rocks. Later Bugge (1943) and Elliot and Morton (1965) interpreted the same rocks as of sedimentary origin. More recently, one of the models for nodular gneisses formation is based on deformation of granites (Hunter and Andronicos, 2013; McLelland et al., 2002b). From the Cooma Complex (Australia) and Adriondack Mountains (North America), Vernon (1979) and McLelland et al. (2002a) attributed the formation of sillimanite to alkali leaching by hydrothermal fluids, while Spry et al. (2022) linked nodular sillimanite rocks of Colorado (North America) to hydrothermal processes and a field indicator to sulphide deposits.

In this study we describe the sillimanite and nodular gneisses of the Proterozoic Bamble lithotectonic domain in south Norway; its field relations, mineral chemistry and microfabric. Textural relationships suggest that the sillimanite gneisses formed by a leaching of K and Mg. Since the intense scapolitisation in the region is induced by K and Mg fluids we suggest that the formation of the sillimanite gneiss interacted by the scapolitisation of the adjacent rocks. Microfabric studies are performed to evaluate the relationship between mineral reactions and deformation, and to characterise deformation mechanism during metasomatism. We discuss the nodular fabric and its origin as a metasomatic rock. We raise the question how metasomatism by chemical rock change during mineral replacement affect rock fabric transformation, and if metasomatism actively contribute to deformation fabric during mass transfer by dissolution-precipitation mechanisms rather than dislocation creep.

2. Geological setting

The Bamble lithotectonic domain (Fig. 1) consist of Proterozoic continental crust reworked during the Sveconorwegian orogeny (e.g., Bingen et al., 2008), considered as one of the classical examples of high-grade metamorphic terranes recording the transition from amphibolite to granulite facies (e.g., Touret, 1971). Based on garnet-orthopyroxene gneisses regional metamorphic conditions is estimated to $T > 850$ °C and P up to 1.15 GPa (Engvik et al., 2016). The Bamble lithotectonic domain, together with the Modum-Kongsberg domain (Fig. 1), includes a series of metasomatic rocks. Scapolite metagabbros, where scapolite coexisted with enstatite, phlogopite, amphibole and rutile, is constrained at 600 to 700 °C at mid-crustal levels (Engvik et al., 2011; Lieftink et al., 1994; Munz et al., 1994). Mg-Al-rich lithologies, i.e., orthoamphibole-cordierite schists and sillimanite gneisses occur together with scapolitised rocks (Engvik and Austrheim, 2010; Munz et al., 1994), estimated to have been formed at $T > 930$ °C and 1.0 GPa by Kihle et al. (2010). Dolomite-carbonates were deposited by carbonitisation (Dahlgren et al., 1993). Albitisation is widespread, broadly affecting the Mesoproterozoic rocks of the Sveconorwegian orogen in southern Scandinavia (Fig. 1; Nijland et al., 2014, Munz et al., 1994, Engvik et al., 2014). The Bamble and Modum-Kongsberg lithotectonic

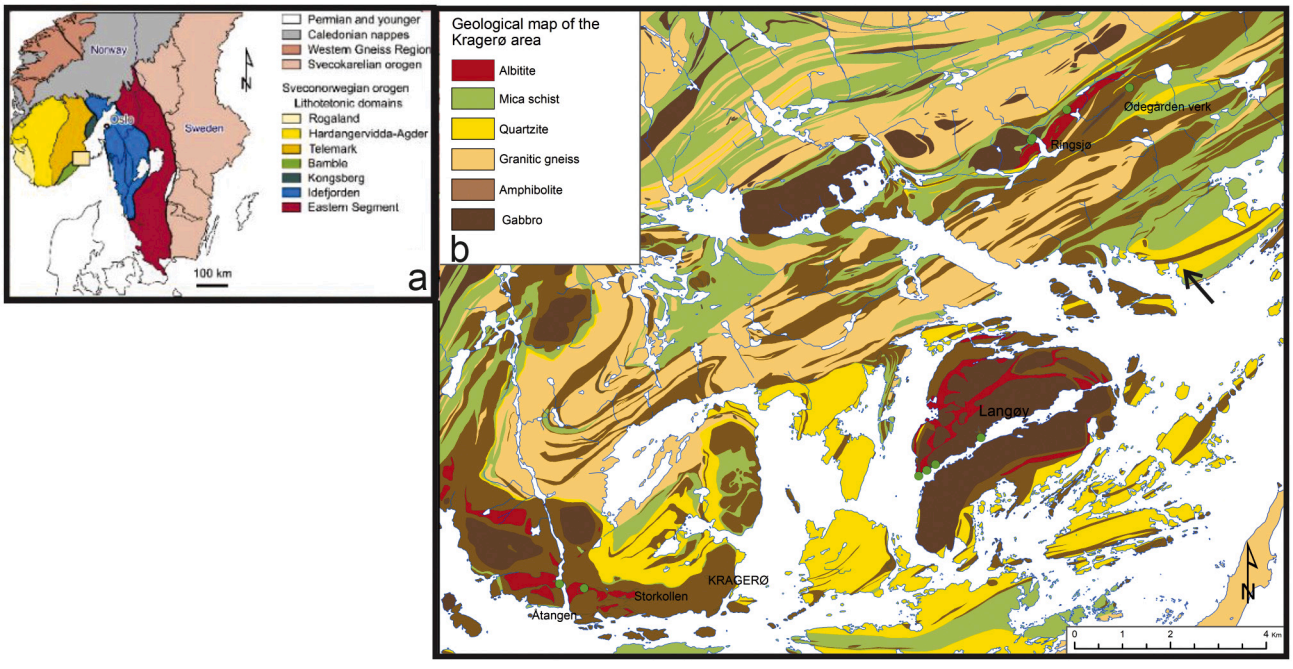

Fig. 1. a) Regional tectonic map of South Norway, square indicates study area enlarged in Fig. 1b (from Engvik et al., 2016) b) Geological map of the Kragerø-Bamble area of the Bamble lithotectonic domain, South Norway (after Engvik et al., 2018). Arrow indicates sampled area.

domains are situated bordering to the magmatic active Permian Oslo Rift (Fig. 1), and Austrheim et al. (2022) links part of the Na-metasomatism and low-grade alteration to the Permian activity.

3. Metasomatism in the Bamble lithotectonic domain by K-Mg-Cl rich fluids

The infiltration of Mg-K-Cl-fluid was important during the metasomatism of the Bamble lithotectonic domain. Engvik et al. (2011) and Kusebauch et al. (2015a) documented Mg-K-Cl-metasomatism as critical during transformation of gabbros to scapolite metagabbro. Cl is the major component of the marialitic scapolite in the Kragerø-Bamble area (Engvik et al., 2011; Me_{19-42}, Cl < 0.97 a.p.f.u.). The infiltration of Cl was in special important during formation of this areas characteristic Ødegården chlorapatite (Brøgger and Reusch, 1875) and its extensive deposits (Engvik et al., 2009; Harlov et al., 2002; Kusebauch et al., 2015b; Lieftink et al., 1994; Nijland et al., 1993). Lieftink et al. (1994) and Harlov et al. (2002) highlighted the importance of Cl during mobilization of rare earth elements in the apatite. K-Mg-rich fluids were transforming Fe-Ti oxides to phlogopite, biotite and talc (Austrheim et al., 2008), and the K-Mg-rich phlogopite is a modally important part of both the scapolite metagabbros and the extensive chlorapatite veins. Mg-infiltration caused formation of sapphirine and corundum in metasomatized gabbros, a process that were discussed as important for formation of Mg-Al-rich lithologies as orthoamphibole-cordierite schists (Engvik and Austrheim, 2010). Chlorine is an active ligand in hydrothermal fluids (Liebscher, 2007), transforming both mafic and felsic rocks into albitites during Na-metasomatism (Engvik et al., 2008, 2014, 2017; Nijland et al., 2014). Stable isotopic studies from the Bamble-Kragerø area indicate marine evaporites or a seawater source for the Cl-bearing fluid (Bast et al., 2014; Engvik et al., 2018). Chlorine is effectively depleting Fe and a transport and canalization by hydrothermal fluids can explain the ore deposition in the Bamble lithotectonic domain (NGU Ore Database; Engvik et al., 2014).

4. Analytical methods

Thin sections of selected samples represent slices parallel to the sample lineation (x) and perpendicular to the foliation (z). Detailed petrographic studies were performed by optical microscopy and scanning electron microscopy (SEM) using a LEO1450 VP instrument at the Geological Survey of Norway (NGU). Mineral identification was done with an energy-dispersive spectrometer (EDS) mounted on the SEM. Analythical conditions were 10 nA sample current, 15 kV acceleration voltage and working distance 7 mm. An overview of key samples with mineral assemblage, replacement reaction and major fabric are listed in Table 1.

For electron backscattered diffraction (EBSD) analytics at the scanning electron microscope (SEM), the thin sections were polished using a colloidal silica suspension (Syton, 0.02–0.06 μm) in a vibratory polisher for 2 h and coated with a thin (5–7 nm) carbon layer. The samples were analysed with a Hitachi SU5000 field emission SEM equipped with a Nordlys II EBSD detector and integrated with EDS (Oxford Instruments) at the Department of Earth and Environmental Sciences at LMU Munich. For acquisition and interpretation of data, the AZtec software 4.2. and for processing of EBSD data the Channel 5 software of Oxford Instruments was used. EDS measurements were taken at 20 kV and a working distance of 10 mm. Automatic EBSD measurements were taken at 20 kV using a pre-tilted sample holder (70°) with working distances between 10 and 20 mm and step sizes of 1.6 to 3 μm. The presented pole figures represent stereographic projections of the lower hemisphere.

The bulk rock compositions (Table 2) were analysed at NGU, measured on tablets and fused glass beads prepared by 1:7 dilution with lithium tetraborate. The samples were analysed on a PANalytical Axios XRF spectrometer equipped with a 4 kW Rh X-ray end-window tube, using common international standards for calibration.

Quantitative microanalyses of minerals (Table 3) were performed using a Cameca SX100 electron microprobe equipped with 5 wavelength-dispersive spectrometers (WDS) at the Institute of Geosciences, University of Oslo. The accelerating voltage was 15 kV and the counting time 10 s on peak using a beam current of 15 nA. K-feldspar was analysed with a focused beam, while a defocused bean of 5–10 μm was used for the micas. Standardization was made on a selection of synthetic and natural minerals and oxides. Data reduction was done by the PAP program (Pouchou and Pichoir, 1984). Structural formula for K-feldspar is calculated on the basis of five cations, and for micas based on 22 oxygen. Mg# are calculated as Mg/(Mg + Fe).

5. Field relations and rock characteristics

The Kragerø-Bamble area (Fig. 1) consists of an interlayered complex of mafic rocks and variable gneisses and quartzites (Padget and Brekke, 1996). The mafic rocks are amphibolite and metagabbro including scapolite metagabbro, bodies of gabbro, interlayered by Mg-rich

Table 1
Key samples (abbreviations after Whitney and Evans, 2010).

Sample No.	*E*-UTM	N-UTM	Rock type	Major minerals	Minor minerals	Accessory minerals	Replacement reactions	Fabric
AE4	532,131	6,532,620	Biotite gneiss	Qz Bt	Wm Kln	Opq	Bt= Fe-oxide+prehnite; Kln; Kfs= Wm	Well-developed foliation
AE123	532,016	6,532,464	Sillimanite nodular, well-foliated gneiss	Sil Qz Bt				Well-developed foliation in layers
AE124	532,067	6,532,556	Sillimanite nodular gneiss	Sil Qz	Bt Kfs Wm Kln Chl Sil Wm Pl	Tur Zrc Opq Opq Green-Spl	Bt= Wm + Kln + Chl + Fe-oxide	Well-developed foliation
AE125	532,042	6,532,726	Sillimanite-mica gneiss	Qz Kfs Bt	Prh	Zrc Ap	Bt= Fe-oxide+prehnite; Kfs= Wm	Weak foliation
AE126	532,131	6,532,620	Sillimanite nodular and foliated gneiss	Sil Qz Bt Wm Kfs	Chl Kln	Tur	Kfs= Wm; Bt= Chl + Kln	Variable foliation
AE127	532,131	6,532,620	Sillimanite-mica gneiss	Sil Qz Bt	Kfs Wm Chl	Zrc	Bt= Chl; Kfs= Wm	Variable foliation
AE128	532,131	6,532,620	Sillimanite nodular gneiss	Sil Qz Bt	Wm	Opz Zrc	Bt= Wm + Fe-oxide; Fld-breakdown	Well-developed foliation
AE129	532,131	6,532,620	Sillimanite nodular gneiss	Sil Qz Bt Wm Kfs			Kfs= Wm; Cc; Wm= Sil	Variable foliation in laysers
AE130	532,187	6,532,584	Sillimanite gneiss	Sil Qz	Bt Wm Chl Kfs Wm Pl	Opq Zrc Ap	Bt= Chl + Wm + Fe-oxide; Wm= Sil	Well-developed foliation, partly large-grained quartz
AE132	532,007	6,532,752	Sillimanite-mica gneiss	Sil Qz Bt	Prh	Opq Zrc Ap	Bt= Phrenite+Fe-oxide; Wm= Sil; Kfs= Wm	Variable foliation
AE133	531,909	6,532,853	Biotite gneiss	Qz Bt	Kfs Wm	Opq Zrc	Bt= Wm + Fe-oxide: Kfs= Wm	Well-developed foliation

Table 2
Whole rock geochemistry.

Sample No	Rock type	SiO_2	Al_2O_3	FeO*	TiO_2	MgO	CaO	Na_2O	K_2O	MnO	P_2O_5	LOI	Sum	ASI **	Fe-index***	Na_2O + K_2O-CaO
AE4	Biotite gneiss	76.70	8.57	3.31	0.52	5.13	0.21	0.05	4.18	0.02	0.01	1.21	98.70	1.79	0.39	4.02
AE123	Sillimanite nodular, well-foliated gneiss	91.70	4.04	1.01	0.24	1.22	0.14	0.05	1.01	0.02	0.06	0.64	99.50	3.11	0.45	0.92
AE124	Sillimanite nodular gneiss	90.60	5.07	0.60	0.12	0.52	0.15	0.18	1.94	0.01	0.04	0.75	99.30	2.00	0.54	1.97
AE125	Sillimanite-mica gneiss	73.90	13.10	2.24	0.28	1.47	0.68	1.10	6.76	0.02	0.06	1.10	99.60	1.34	0.60	7.18
AE126	Sillimanite nodular and foliated gneiss	82.90	9.44	1.10	0.21	2.03	0.17	0.14	2.24	0.05	0.04	1.79	98.30	3.36	0.35	2.21
AE127	Sillimanite-mica gneiss	83.10	8.34	1.25	0.30	2.72	0.12	0.14	3.19	0.01	0.05	1.44	99.20	2.20	0.31	3.22
AE128	Sillimanite nodular gneiss	81.30	9.03	2.05	0.32	2.80	0.10	0.14	3.30	0.01	0.05	1.15	99.10	2.32	0.42	3.34
AE129	Sillimanite nodular gneiss	83.00	9.78	1.43	0.24	1.32	0.40	0.25	2.80	0.05	0.06	1.55	99.30	2.57	0.52	2.65
AE130	Sillimanite gneiss	93.50	3.33	0.45	0.11	0.41	0.12	0.05	0.98	0.05	0.05	0.66	99.00	2.66	0.52	0.91
AE132	Sillimanite-mica gneiss	81.90	9.80	1.39	0.27	1.11	1.36	0.40	2.69	0.02	0.08	1.04	99.00	2.04	0.56	1.73
AE133	Biotite gneiss	80.20	10.00	1.92	0.36	2.62	0.14	0.14	4.29	0.01	0.07	1.27	99.80	2.00	0.42	4.29

* FeO = FeOtotal.
** ASI = Aluminum Saturation Index (Al / (Ca – 1.67*P + Na + K)).
*** Fe-index = FeOtot/(FeOtot+MgO).

Table 3
Representative mineral chemical data.

Sample No.	AE126B	AE126B	AE126B	AE126B	AE126B	AE124
Analyse No.	#12	#11	#21	#14	#19	#24
Mineral phase	K-feldspar	Biotite	Biotite	Muscovite	Muscovite	Muscovite
SiO_2	64.89	38.80	37.01	49.86	47.19	47.20
TiO_2	0.00	2.09	2.31	0.01	0.02	0.01
Al_2O_3	18.42	20.13	19.04	31.42	34.55	33.18
FeO	0.00	6.80	12.73	1.66	0.83	1.94
MnO	0.00	0.03	0.10	0.01	0.00	0.00
MgO	0.01	17.04	13.14	1.75	1.24	1.24
CaO	0.02	0.00	0.01	0.07	0.39	0.01
Na_2O	2.60	0.09	0.13	0.09	0.19	0.14
K_2O	13.39	9.30	9.76	10.33	8.26	11.07
Cr_2O_3	0.03	0.00	0.02	0.00	0.00	0.00
Total	99.34	94.43	94.24	95.20	92.62	94.78
	*	**	**	**	**	**
Si	2.98	5.56	5.51	6.61	6.33	6.34
Ti	0.00	0.23	0.26	0.00	0.00	0.00
Al	1.00	3.40	3.34	4.91	5.47	5.25
Fe	0.00	0.82	1.58	0.18	0.09	0.22
Mn	0.00	0.00	0.01	0.00	0.00	0.00
Mg	0.00	3.64	2.91	0.35	0.25	0.25
Ca	0.00	0.00	0.00	0.01	0.06	0.00
Na	0.23	0.02	0.04	0.02	0.05	0.04
K	0.79	1.70	1.85	1.75	1.41	1.90
Cr	0.00	0.00	0.00	0.00	0.00	0.00
Sum cations	5.00	15.37	15.51	13.82	13.66	14.00
Mg/(Mg + Fe)	–	0.82	0.65	0.65	0.73	0.53
Kfs	0.77					
An	0.00					
Ab	0.23					

* structural formula based on 5 cations.
** structural formula based on 22 O.

orthoamphibole-cordierite amphibolitic schist. Granitoid gneisses are of granitic, granodioritic, quartzdioritic, and tonalitic composition. Albitite occur as larger bodies or vein alteration cutting through both mafic, granitoid and felsic rocks. Quartzite is interlayered with garnet amphibolite, granitoid gneisses, and garnet- and cordierite-bearing mica gneiss. The quartzite is extensive and following the main structural trend of the area (Padget and Brekke, 1996; Fig. 1) and contain variable amounts of sillimanite and occurs partly as nodular and foliated sillimanite gneisses (Brøgger, 1934; Bugge, 1943; Elliot and Morton, 1965). The relationship between the Mg-K rich scapolite metagabbro, Mg-rich orthoamphibole-cordierite amphibolitic schist and sillimanite nodular gneisses is evident, i.e., by the localities Ringsjø (Fig. 1; Engvik and Austrheim, 2010) and Åtangen (Fig. 2a).

The sillimanite gneisses were studied and sampled in detail at the Valle locality in the Kragerø-Bamble area (Fig. 1) where the lithology occurs as a c. 800 m thick layer included in various quartzite and mica-rich gneisses. The sillimanite-bearing gneiss are showing peculiar nodular structures (Fig. 2b). The nodules are a few-cm large spherical to

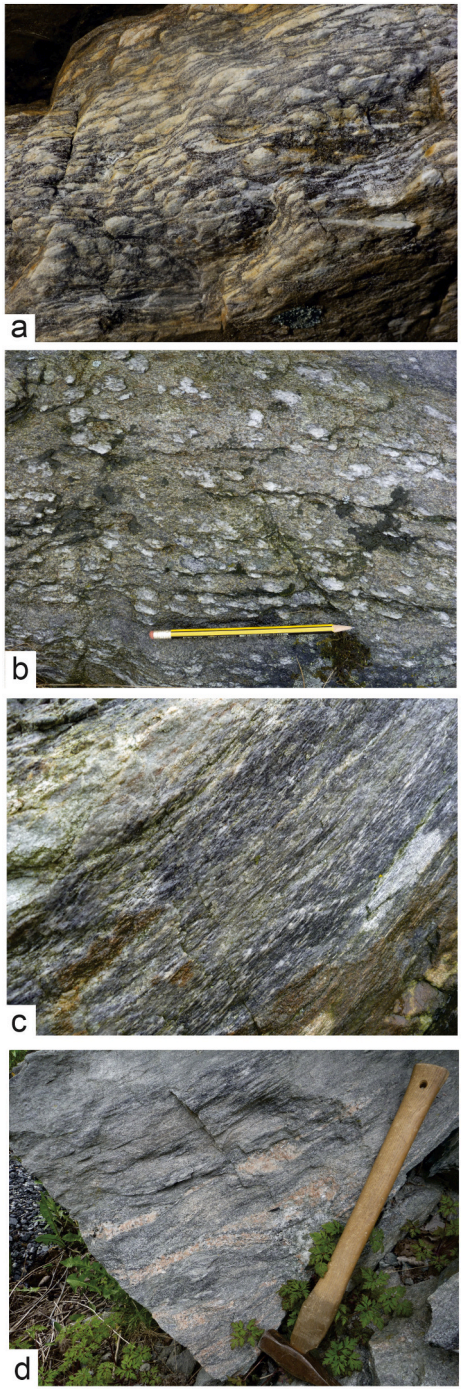

Fig. 2. Field photos, Bamble lithotectonic domain: a) 0.5 m thick layer of sillimanite-nodular gneiss in the orthoamphibole-cordierite-bearing amphibolite at locality Åtangen. b) Sillimanite-nodular gneiss, locality Valle. c) Foliated sillimanite-bearing gneiss, locality Valle. d) K-feldspar-layers in mica-rich gneiss, locality Valle.

slightly elongate aggregates of quartz and sillimanite. The sillimanite gneisses show a variable degree of foliation. The elongation of the spherical nodules forms a lineation flattened into the foliation. The sillimanite gneiss varies spatially with layers including preserved nodules between horizons where the nodules are aligned in the foliation as a variable sillimanite-mica-quartz-K-feldspar gneisses, grading into well-foliated sillimanite gneiss (Fig. 2c). The sillimanite gneisses can contain K-feldspar-rich layers (Fig. 2d).

5.1. Geochemical composition

The geochemical composition of the major elements in Table 2 and Fig. 3 illustrates the rocks peraluminous composition. Both biotite gneisses and sillimanite-bearing gneisses are silica-rich (76–94 wt% SiO_2) with an aluminum saturation index (ASI = Al/(Ca-1.67P + Na + K)) >1.0 for all samples (Fig. 3a). The alkali and calcium content (Na_2O + K_2O + CaO) show a broad general variation of 0.9–7.2 wt% for the measured samples (Fig. 3b). Both Na_2O and CaO occur low, while K_2O shows a variation, at highest up to 6.8 wt%, contributing to the spread (Fig. 3b). The Fe-index ($FeO^{tot}/(FeO^{tot} + MgO)$; Frost et al., 2001) varies from 0.31 to 0.60, which confirm magnesian character for high SiO_2 compositions. (Fig. 3c).

6. Mineral chemistry and reaction microfabrics

The sillimanite- and nodular gneisses are quartz-dominated with various modal contents of K-feldspar, sillimanite, white mica and biotite. Plagioclase occurs only locally and minor, and zircon, tourmaline, apatite, spinel and Fe-oxide accessory (Table 1). K-feldspar is $Kfs_{77}Ab_{23}$, biotite is Mg-rich (Mg# = 0.65–0.82; Ti = 0.23–0.26 a.p.f.u.) and white

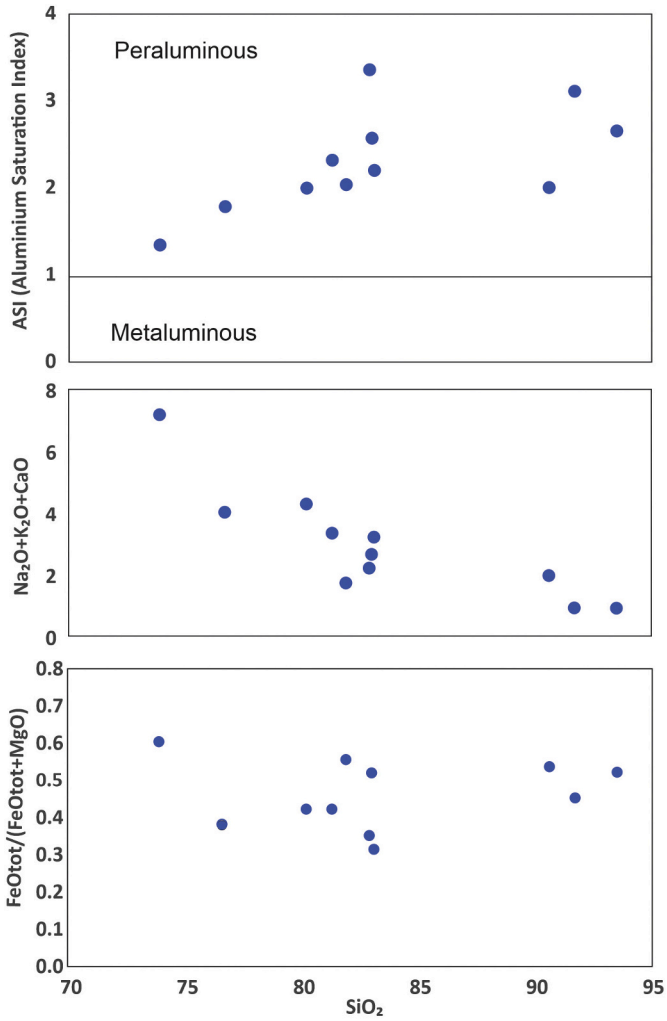

Fig. 3. Geochemical characteristics of nodular and sillimanite gneiss, major elements: a) The aluminum saturation index (ASI) plot (after Maniar and Piccoli, 1989) shows a peraluminous composition of the sillimanite-bearing gneisses. b) Na + K + Ca composition versus SiO_2 plot illustrates a lowering with increasing SiO_2 content. c) Fe-index versus SiO_2 illustrates a magnesian composition (Frost et al., 2001) of the sillimanite gneisses.

mica is muscovite with Si = 6.33–6.61 a.p.f.u. (Table 3). The rocks show different reaction fabrics and microfabrics, which are described as follows:

I – Biotite-breakdown reaction fabrics: Biotite is typically aligned with its basal plane in the foliation (Fig. 4 a-c). It can be partly replaced by muscovite, present along the cleavage plane of biotite (Fig. 4). Muscovite can also occur along microfractures in biotite (Fig. 4d). Associated are small Fe-oxides along the cleavage planes (Fig. 4) but also along microfractures or phase boundaries of muscovite and biotite (Fig. 4e-f).

II – K-feldspar-breakdown reaction fabric: Coarse (few hundred μm in diameter) K-feldspar, quartz and biotite crystals are aligned within the foliation plane (Fig. 5a). K-feldspar can be partly (Fig. 5 a, c, d) or completely replaced by fine-grained aggregates of white mica (Fig. 5 b, e, f). The different grey scale in BSE-image of the fine-grained white mica aggregate (Fig. 5f) reflects minor variations in the content of Al and K versus Mg and Fe. Roundish quartz inclusions are common in the muscovite aggregates (Fig. 5b, e).

III – Sillimanite growth fabrics: Sillimanite needles occur both in sillimanite-rich layers parallel to the foliation and as fibrous crystals included in quartz and muscovite (Fig. 6). They show typically a few μm thickness and a few tens of μm length. Sillimanite is found as irregular aggregate replacing white mica (Fig. 6c-f, 7a-b).

IV – Muscovite microfabric: Muscovite forms several hundred μm long elongate crystals, typically a few tens of μm wide with an aspect ratio of ca. 5:1 (Fig. 6c-d, 7a-b). Generally, phase boundaries dominate, which are mostly lobate and thus irrational (Fig. 6c-f, 7a-b, 8a-c), i.e., they are not dominated by the cleavage plane (the basal plane). Micas included in quartz show similar crystallographic orientations, which is interpreted as representing coarse grains connected in 3D and is not indicating a preferred orientation associated to the foliation (Fig. 7).

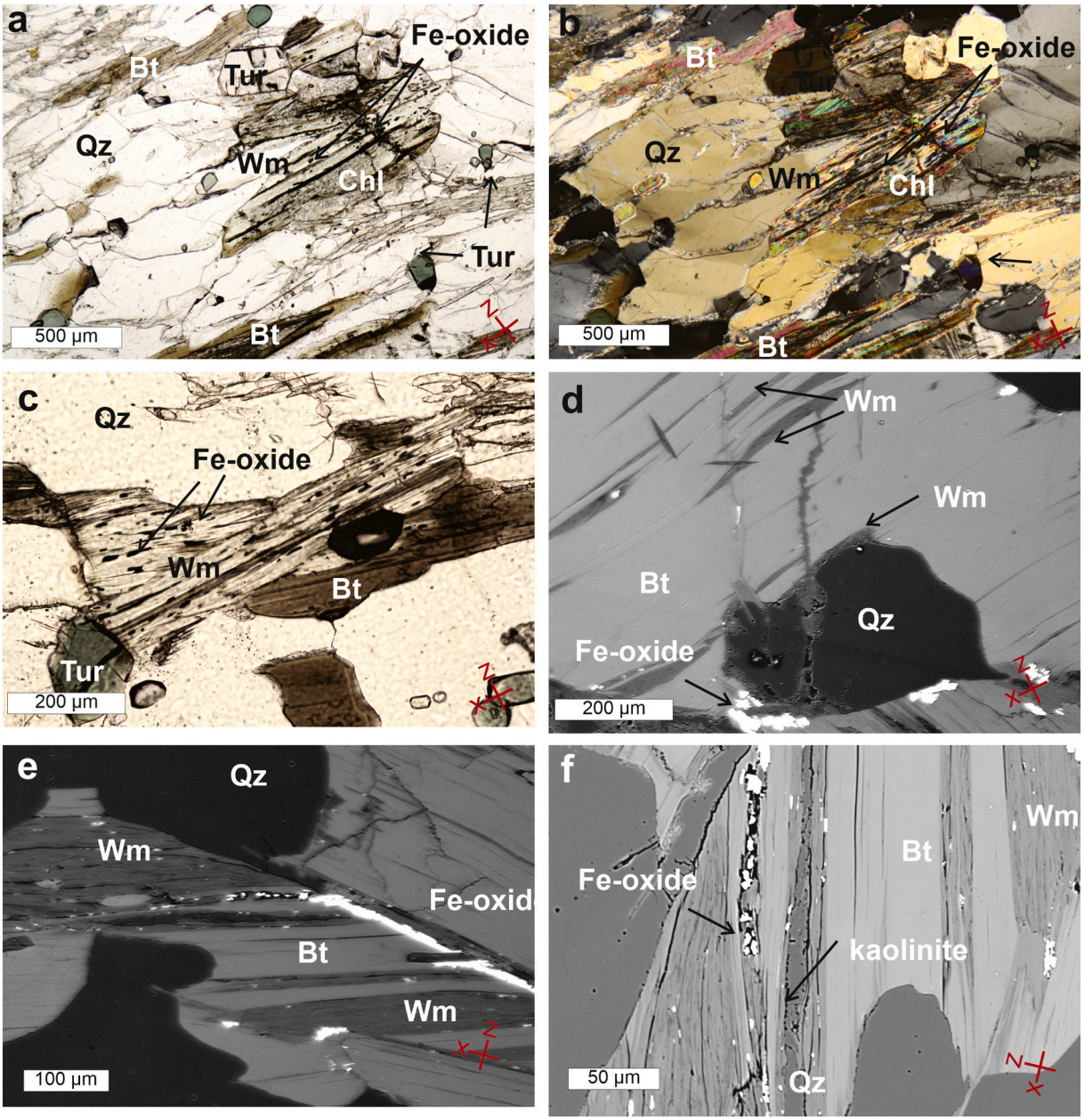

Fig. 4. Biotite replacement microfabrics (abbreviations after Whitney and Evans, 2010): (a-c) Biotite and white mica occur in alternating lamellas parallel to the cleavage plane, along which also Fe-oxide and locally some chlorite occurs. Sample AE126, photomicrograph (b taken with crossed polarizers). (d-f) White mica occurs along cleavage planes of biotite and along microcracks through biotite and quartz. Fe-oxide is present along grain boundaries and associated with white mica. Locally, kaolinite is observed along the cleavage planes in biotite. Sample AE4, BSE-images.

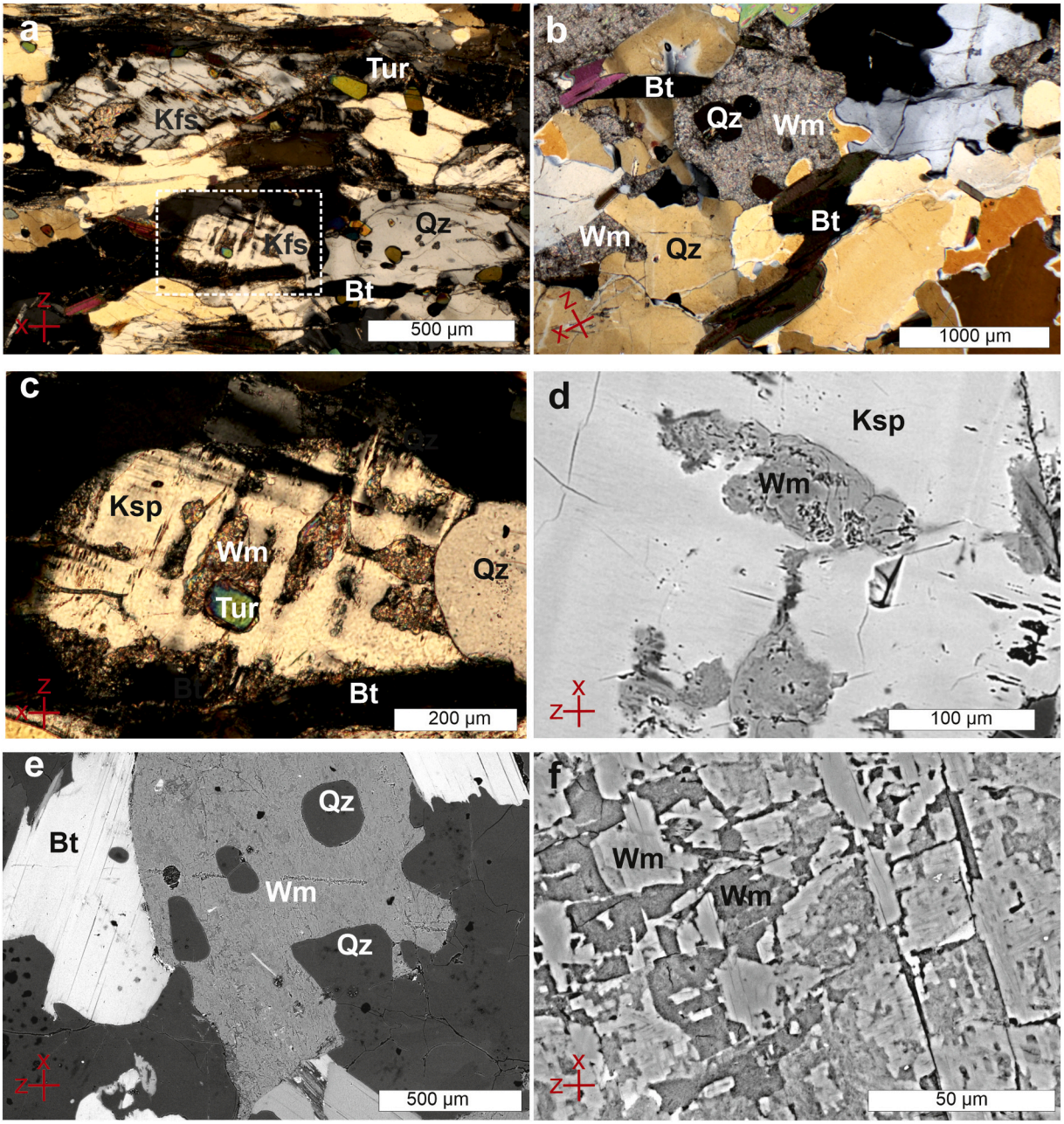

Fig. 5. K-feldspar breakdown microfabrics. (a-c) K-feldspar showing various replacement to white mica. Photomicrographs, sample AE126, crossed polarizers (c is closeup of area marked in (a) by white-dashed line). (d) K-feldspar showing white mica along microcracks within the crystal. BSE-image, sample AE126. (e) Former K-feldspar completely replaced by fine-grained white mica with included quartz. Note lobate phase boundaries to quartz. BSE-image, sample AE129. (f) Fine-grained aggregate of white mica, as replacement of K-feldspar. Different grey scale reflects smaller variation in the mineral chemistry. BSE-image, sample AE129.

V – Nodules: The sillimanite nodules, peculiar in outcrop scale (Fig. 2b), are in microscale constituted by mainly quartz and sillimanite (Fig. 6a-b). Quartz grains are sub- to anhedral and varying in grain size from 0.5 to 2 mm. The quartz has a variable shape-preferred orientation (SPO). Sillimanite crystals occur along quartz grain boundaries but also included in quartz and mica (Figs. 6, 7a-b, 8).

VI – Foliation: The foliation is characterized by alternating quartz-rich, sillimanite-rich and/or mica-rich layers (Fig. 8e-f). Whereas muscovite shows a shape but not an associated crystallographic orientation and lobate phase boundaries (Fig. 8a-c), biotite is showing rational phase boundaries with its cleavage plane aligned into the foliation (Fig. 9e-f). Quartz is medium- to coarse-grained and has a shape-preferred orientation with the long axis of grains of a few hundred µm aligned in the foliation and a typical aspect ratio 4:1. Quartz commonly forms so-called ribbon grains characterized by elongate grains with a width of 50–100 µm and an aspect ratio of 4:1. (Figs. 8b-d, 9), where the long axis of grains, i.e., the ribbon boundary, is typically a phase boundary (to sillimanite and/or mica) and the short axis of grains is a grain boundary at high angle to the ribbons (Figs. 8d, 9a, c). Low-angle grain boundaries are rare in the ribbons and quartz shows typically a low relative misorientation (the average grain orientation spread is lower than 3°, Fig. 9c). There is no apparent crystallographic preferred orientation of quartz (Fig. 9b). Sillimanite-crystals are elongated with a marked SPO and associated crystal-preferred orientation (CPO) characterized by the ⟨001⟩ direction within the foliation plane (Fig. 9).

VII – Retrograde mineral reactions:

Retrograde mineral reactions are indicated by typical low-grade minerals as chlorite, kaolinite, prehnite and pumpellyite occurring as

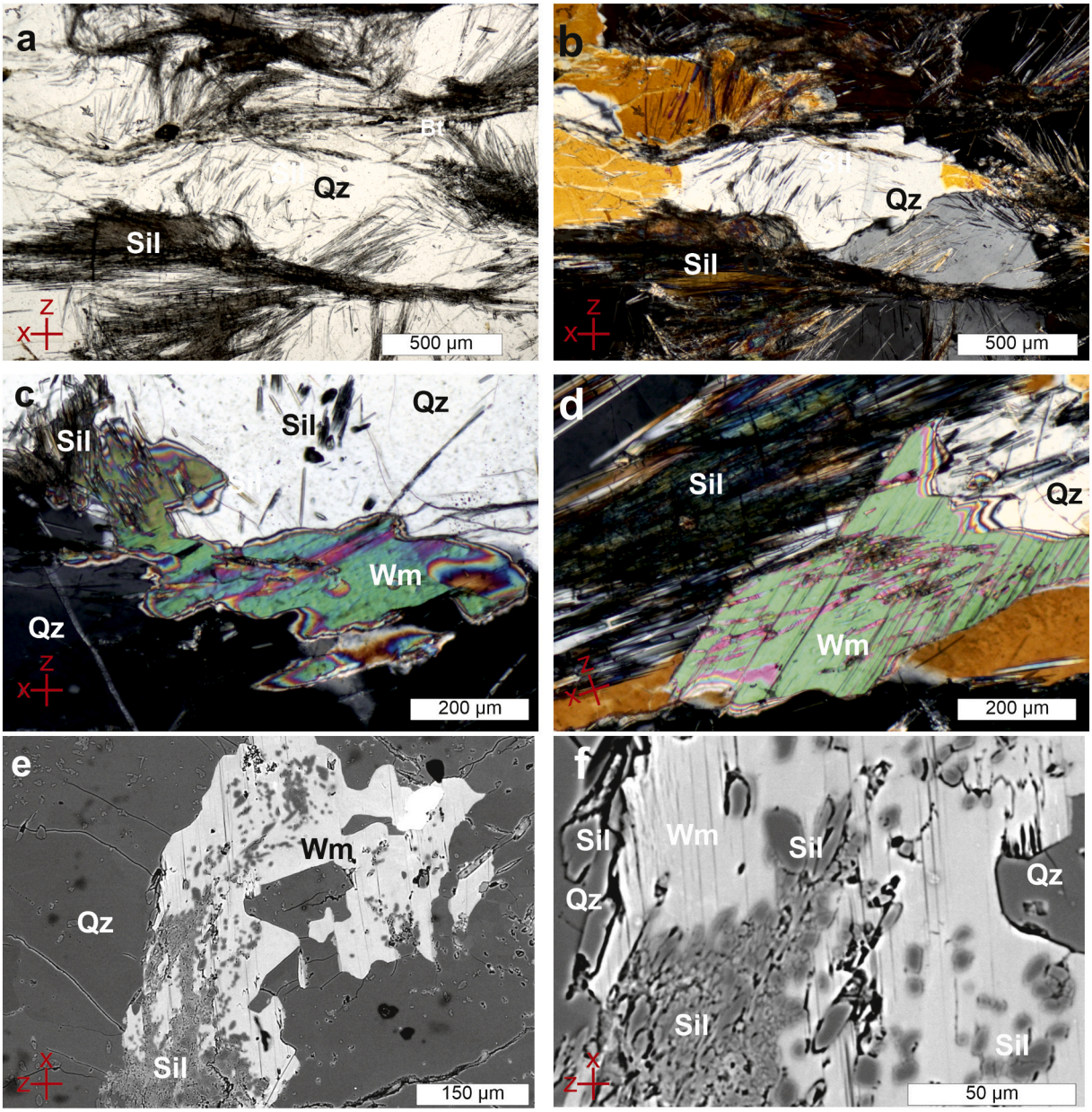

Fig. 6. Sillimanite growth microfabrics. (a, b) Sillimanite as thin needles included in quartz. Sample AE126, photomicrographs, b) taken with crossed polarizers. (c, d) Sillimanite needles included in quartz and muscovite. Note the lobate phase boundaries of white mica. Sample AE129, photomicrographs, crossed polarizers. (e, f) Sillimanite replacing white mica. BSE-image, sample AE129.

lamellas commonly included in biotite or within microscale veins (Table 1, Fig. 4a-b, f). Sillimanite show partly a late alteration to sericite. The low-grade facies minerals and reactions from the region are described in detail by Austrheim et al. (2022).

7. Discussion

7.1. Mineral reactions

Assuming immobile Al, the observed replacement of biotite by muscovite can be written as:

$$3\text{Biotite} \rightarrow \text{muscovite} + 9\,(\text{Fe, Mg}) + 2\,\text{K} + 6\,\text{quartz} + 2\,\text{H}_2\text{O} \quad (1)$$

$$3\,\text{K(Mg, Fe)}_3(\text{AlSi}_3\text{O}_{10})(\text{OH})_2 \rightarrow \text{KAl}_2(\text{AlSi}_3\text{O}_{10})(\text{OH})_2 + 9\,\left(\text{Fe}^{2+}, \text{Mg}^{2+}\right) + 2\,\text{K}^{+} + 6\,\text{SiO}_2 + 2\,\text{H}_2\text{O}$$

The replacement of biotite to muscovite releases Fe, Mg, K, SiO_2 and water (Fig. 10). The muscovite partly replacing biotite occurs along the cleavage planes (Fig. 4). SiO_2 is conserved as quartz and the excess of Mg and K is interpreted to be released in the fluid. Fe is represented by Fe-oxide; Fig. 4 illustrates Fe-oxide along mica cleavage planes and grain boundaries (Fig. 4a-e) as well as in the replacement product of muscovite (Fig. 4e-f). Muscovite (Fig. 4d) and Fe-oxide (Fig. 4f) along microcracks and Fe-needles along grain boundaries (Fig. 4e) indicate Fe-mobility by channelized fluid flow. Assuming transportation of the released elements and water, the reaction leads to a molar volume loss of 39%, according to the molar volumes of biotite (c. 151/cm^3), muscovite (141/cm^3) and quartz (23/cm^3; molar volumes based on Robie and Bethke, 1962).

The observed replacement of K-feldspar to muscovite and sillimanite can be described by a two-staged quartz and potassium-producing mineral reaction: In the first stage, by infiltration of water (possibly

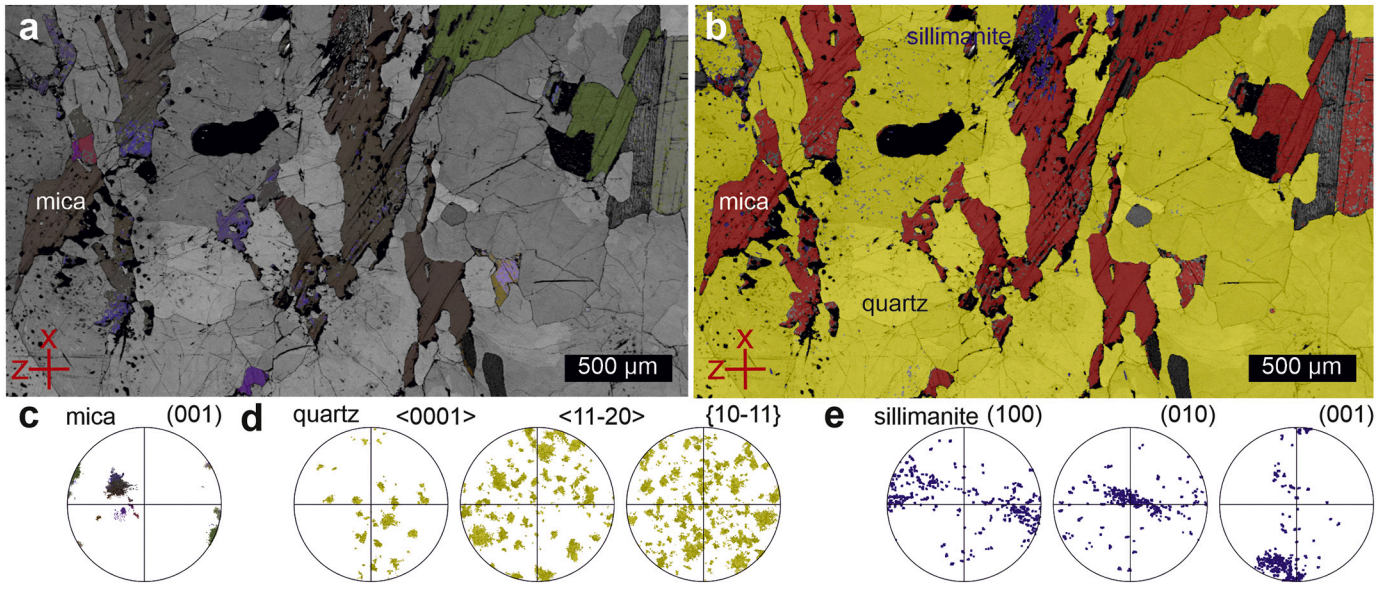

Fig. 7. EBSD data of quartz-mica aggregates (sample AE 129). (a) Micas are colour coded by crystallographic orientation (three Euler angles) overlying band contrast. (b) Phase map with quartz in yellow, mica in red and sillimanite in blue colours. (c-e) Pole figure of crystallographic orientations of mica, quartz and sillimanite planes and directions, colour coding and orientation correspond to the map in (b). Note the similar orientation of mica in (a) and the missing association of the long axes of mica to the orientation of the basal plane of mica and the lobate phase boundaries. (For interpretation of the references to colour in this figure legend, the reader is referred to the web version of this article.)

partly released due to the breakdown of biotite), K-feldspar breaks down to white mica where K-feldspar is replaced to muscovite in micro-fractures through K-feldspar (Fig. 5a, c-d), or as a complete replacement and pseudomorph after K-feldspar (Fig. 5b, e-f):

$$3\ \mathrm{K-feldspar} + \mathrm{H_2O} \rightarrow \mathrm{white\ mica} + 6\ \mathrm{quartz} + 2\ \mathrm{K} \quad (2)$$

$$3\ \mathrm{KAlSi_3O_8} + \mathrm{H_2O} \rightarrow \mathrm{KAl_2(AlSi_3O_{10})(OH)_2} + 6\ \mathrm{SiO_2} + 2\ \mathrm{K^+}$$

The reaction produces in addition to muscovite, also substantial amounts of quartz and excess potassium (Fig. 10). The crystallisation of muscovite consumes in addition minor amounts of Fe and Mg. The very fine-grained muscovite crystals with a random orientation are interpreted as an early and incomplete reaction stage where the different intensities on BSE-images reflect smaller variations in chemistry (Fig. 5f). For the reaction (2) a molar volume loss of 15% is achieved assuming transportation of the released K, according to the molar volumes of K-feldspar (c. 109/cm^3), muscovite and quartz.

In the next stage, muscovite breaks down to sillimanite illustrated as the radiating sillimanite-needles with muscovite in quartzite (Fig. 6a-d) and sillimanite replacement in muscovite (Fig. 6e-f):

$$2\ \mathrm{muscovite} \rightarrow 3\ \mathrm{sillimanite} + 3\ \mathrm{quartz} + 2\ \mathrm{K} + 2\ \mathrm{H_2O} \quad (3)$$

$$2\ \mathrm{KAl_2(AlSi_3O_{10})(OH)_2} \rightarrow 3\ \mathrm{Al_2SiO_5} + 3\ \mathrm{SiO_2} + 2\ \mathrm{K^+} + 2\ \mathrm{H_2O}$$

Transformation of K-feldspar produces sillimanite, quartz and is releasing a K-rich fluid. The incomplete breakdown reaction is illustrated by Fig. 6e-f. The molar volume loss of the reaction is 22% assuming transportation of the released K and water, based on the molar volumes of K-feldspar, sillimanite (50/cm^3) and quartz.

White mica produced in reaction (2), can break down producing sillimanite, quartz, additional K and water following reaction (3), which can again trigger the breakdown of K-feldspar (reaction 2). The release of K produces a peraluminous rock, in accordance with the geochemical data (Table 2; Fig. 3).

7.2. Relation between mineral reactions, metasomatism and microfabric development

As introduced above, deformation of rocks can increase the rates of mineral reactions and vice versa, e.g., during incongruent dissolution-precipitation creep (e.g., Wassmann et al., 2011; Wheeler, 1992; Wintsch et al., 2005). Fluids can enhance mineral reaction by brittle deformation (e.g., Jamtveit et al., 2016), or cause change of fabric by dissolution of pre-existing phases and concomitant precipitation of new ones (e.g., Putnis, 2021). All deduced reactions above (reactions 1–3) cause, assuming transportation of released elements and water, a volume reduction. Assuming phase molar volume after Robie and Bethke (1962), the reactions reduce molar volume loss by 15–39% the involved phases, which will enhance rock deformation.

In our study the missing CPO of quartz, the subordinate low-angle grain boundaries and only few sutured high-angle grain boundaries together with the low grain orientation spread, i.e., little internal misorientation of quartz with misorientation angles lower than 5°, reveals that dislocation creep of quartz cannot explain the elongate ribbon-structure of quartz. The formation of quartz-ribbons in high grade metamorphic granulites has been discussed to involve epitactic growth during quartz-producing mineral reactions by diffusional creep (Engvik et al., 2020). Also, the SPO of mica without a corresponding CPO together with the lobate phase boundaries are suggesting, that the foliation is not a secondary foliation formed by rotation of originally homogenously distributed grains into the foliation plane. Coarse muscovite with lobate boundaries to quartz imply low nucleation rates, no crystallographic or surface-energy control during growth and no obvious crystallographic relationship to quartz. Thus, the microfabric shows no evidence of quartz dislocation creep, which implies that bulk stresses at the given pressure/temperature conditions (600 to 700 °C at mid-crustal levels) were not sufficient for a notable accumulation of strain by dislocation creep. Therefore, we can use experimentally calibrated flow laws for dislocation creep of quartz at geological relevant strain rates (e.g., Luan and Paterson, 1992; Tokle et al., 2019) as an upper bound for the stress, which indicates that stresses were below a few tens of MPa. Instead, we interpret the nodular or foliated microfabric to represent growth of muscovite, quartz and sillimanite during

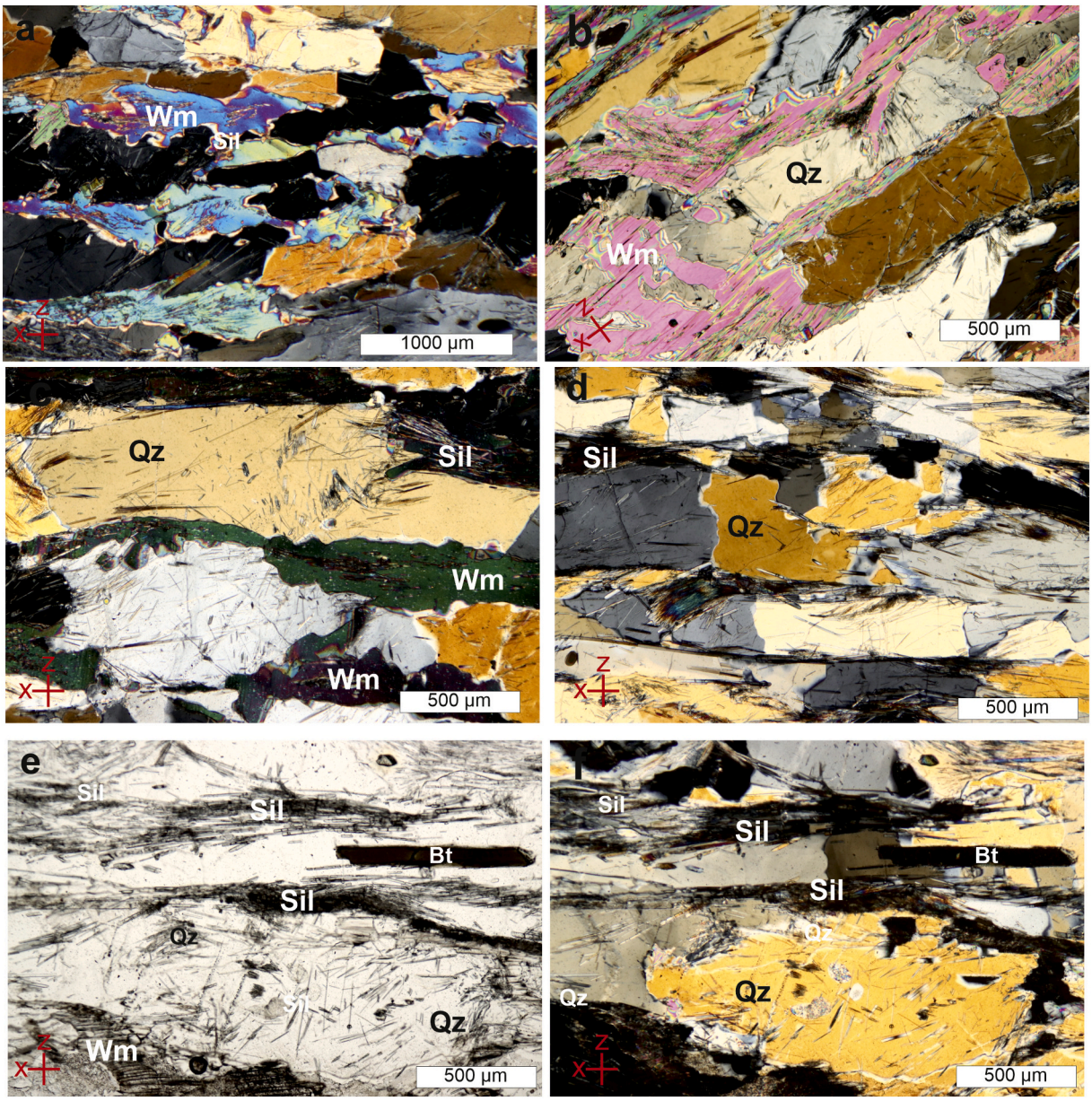

Fig. 8. Polarized light micrographs of foliation microfabric, sample AE129 (a-c, e-f) and AE 123 (d). (a-d) Muscovite with lobate phase boundaries associated with elongate quartz grains aligned in foliation (crossed polarizers). (e, f) Biotite can be present aligned with the basal plane in the foliation plane and rational phase boundaries (f is taken with crossed polarizers).

metasomatic reactions via incongruent dissolution-precipitation creep at low bulk stresses (e.g., Wassmann and Stöckhert, 2013). The difference in microfabric might reflect locally varying stress/strain conditions and possibly heterogeneities in the microfabric of the rock educt. The nodular sillimanite gneisses might represent a coarser educt, whereas the foliated sillimanite gneisses represent a finer grained rock educt. A finer grain size can be expected to lead to a lower viscosity given the polyphase mineral assemblage and fluid availability and therefore accommodating the higher amount of strain, compared to the coarser grain size, given the grain size dependence of dissolution precipitation creep (e.g., Wassmann and Stöckhert, 2013; Wheeler, 1992; Wintsch et al., 2005; Wintsch and Yi, 2002). The metamorphic phase assemblage might have partly inherited the original grain size distribution of the rock educts. Additionally, locally different stress/strain conditions were caused by the volume loss during mineral reactions and associated dissolution-precipitation processes, as described above. Similar deformation and fabric evolution by major element loss during transformation and formation of sillimanite schist are also described Hunter and Andronicos (2013).

7.3. *The origin of K-Mg-metasomatic fluid*

The mineral replacement and deduced reactions above document release of the chemical active K- and Mg-components forming the metasomatic fluid: The breakdown of biotite to muscovite releases K, Mg, Fe, quartz and H_2O (reaction 1). H_2O is reacting with K-feldspar to produce additional amounts of white mica and quartz (reaction 2). During a subsequent reaction muscovite is replaced by sillimanite, again releasing quartz and a K-rich fluid (reaction 3).

The source of fluids is commonly ambiguous when describing fluid-rock interaction and metasomatism and is often difficult to resolve. The scapolite metagabbros of the Bamble lithotectonic domain contain locally a conspicuous high amount of phlogopite (K-Mg-rich mica/biotite). Lieftink et al. (1994) and Engvik et al. (2011) have earlier

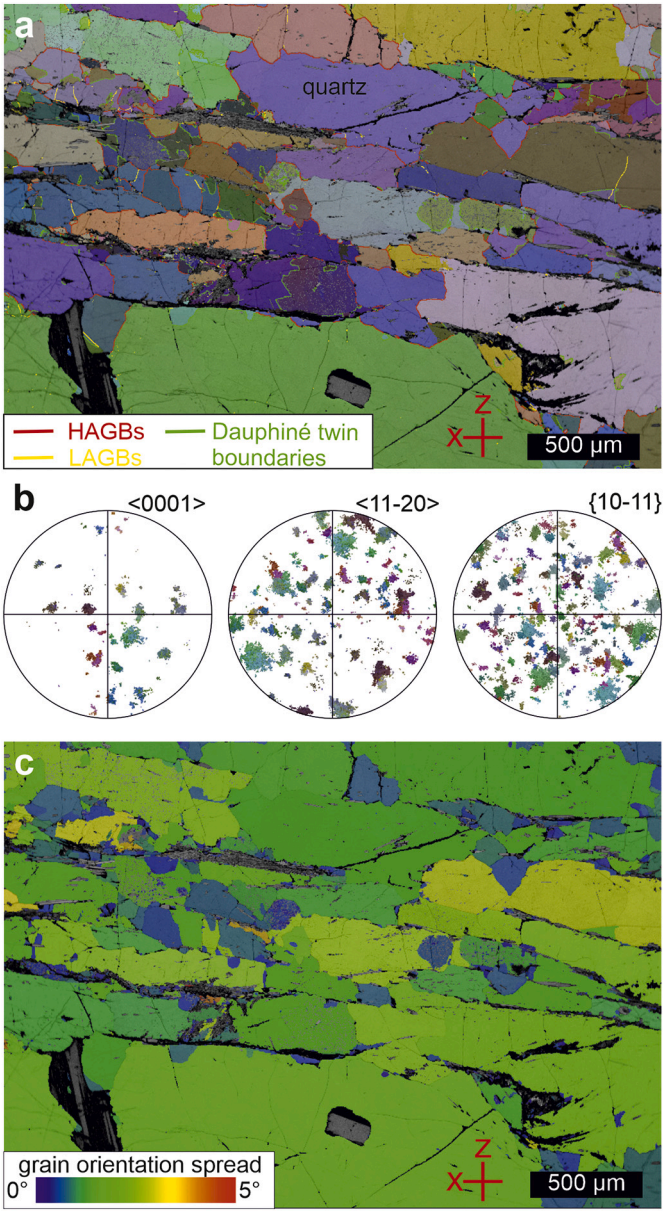

Fig. 9. EBSD data of quartz ribbons separated by sillimanite-rich layers (sample AE 123). (a) Quartz colour coded by crystallographic orientation (three Euler angles) overlying band contrast. Low-angle grain boundaries (<10° misorientation angle) are indicated by yellow lines, high-angle grain boundaries (>10° misorientation angle) by red and Dauphiné twin boundaries are indicated by green lines. (b) Corresponding pole figure for quartz <c> and <a> axes and poles to {r}rhombohedral planes. Colour coding and orientation correspond to the map in (a). (c) Grain orientation spread map showing that relative misorientations are generally below a few degrees. (For interpretation of the references to colour in this figure legend, the reader is referred to the web version of this article.)

documented that this intense scapolitisation was caused by K- and Mg-rich fluids. By this study we now document one possible source of the K-Mg-metasomatic fluid by the breakdown of biotite, K-feldspar and white mica. In addition, the biotite breakdown releases Fe, correlated with tiny Fe-oxide crystals along microfractures and grain boundaries in the restite. As a metasomatic fluid actively transports Fe (Liebscher, 2007), Fe might also be released to the surroundings with an additional contribution to the Fe-deposits in the area (Engvik et al., 2014).

Furthermore, Cl and B are known to be chemical active components during the metasomatism of the Bamble lithotectonic domain by

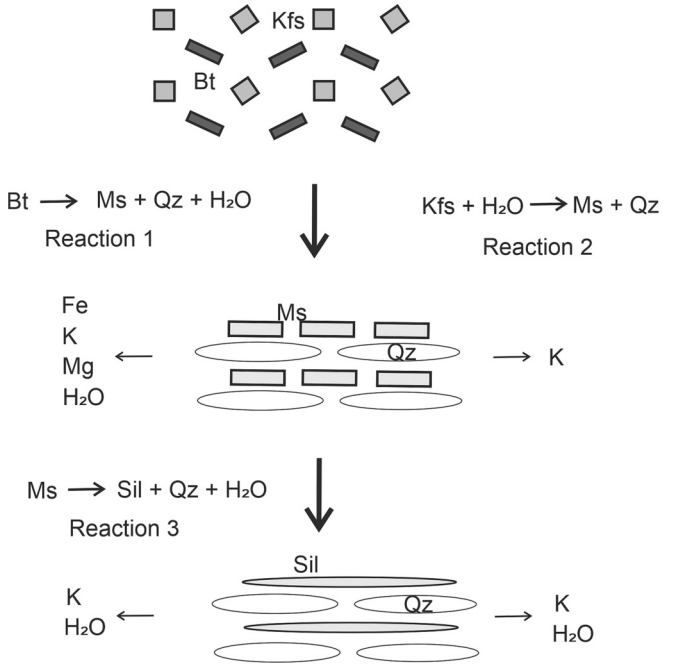

Fig. 10. Simplified overview 2D sketch on the element transport, illustrating evolution of a possible granitic protolith during mineral transformation, metasomatism and evolution of sillimanite gneiss under molar volume loss and isostatic stress. See text for discussion.

extensive occurrence of tourmaline (Bast et al., 2014) and chlorapatite (Engvik et al., 2009; Harlov et al., 2002; Nijland et al., 1993). In the studied sillimanite quartzites tourmaline is a frequent accessory phase (Fig. 5c). Chlorine is an important ligand in hydrothermal fluids and controls solubility and mobility of several metal ions (Liebscher, 2007).

Stable isotopic studies from the Bamble-Kragerø area indicate marine evaporites or a seawater source for the Cl-bearing fluid (Bast et al., 2014; Engvik et al., 2018), while Dahlgren et al. (1993) indicated both magmatic and metamorphic source for the metasomatic fluids. But questions on fluid source can also be discussed in the frame of local or regional source, and the answers will depend on the considered scale. The possible seawater or magmatic source together with increasing temperature could on the regional scale initiate metamorphic reactions. The replacement of biotite (above reaction 1; Fig. 4) illustrates a possible internal source of water that again can initiate breakdown of K-feldspar and white mica to quartz and sillimanite (Figs. 5-6). The documented microfabrics illustrate that the fluid flow is channelled along micro-fractures and grain boundaries (Figs. 4d-f; 5c-d).

8. Conclusions

Our study shows that the nodules of the sillimanite gneiss are mainly comprised by quartz and sillimanite (Fig. 6a-b), formed by the mineral reactions (1–3) where K-feldspar, biotite and white mica in original biotite gneisses are consumed and K-Mg-rich fluids are released (Fig. 10). These fluids documented by the microfabrics of the sillimanite gneisses can explain the intense K-Mg metasomatism of scapolitisation in the Bamble lithotectonic domain.

As introduced above, the presence of sillimanite has been taken as argument in favour of a sedimentary rock origin (e.g., Spry et al., 2022), other studies have assigned their origin in a granitoid environment (Hunter and Andronicos, 2013; McLelland et al., 2002a). The protolith of the Bamble nodular gneiss was most likely a mica gneiss or granite and in accordance with Brøgger (1934), Vernon (1979), McLelland et al. (2002a) and Spry et al. (2022) who attributed sillimanite formation to hydrothermal fluids and alkali leaching.

No evidence of major strain accumulated by dislocation creep was detected to be involved in the microfabric evolution, indicating generally low bulk stress conditions (at the most a few tens of MPa). Instead, we suggest that the nodular or foliated microfabrics formed by incongruent dissolution and precipitation creep depending on the local stress/strain conditions during the mineral replacement reactions (breakdown of K-feldspar and biotite) associated molar volume loss and the microfabric of the rock educt. In this way metasomatism can actively contribute to a deformation fabric during mass transfer and molar volume change. Our study demonstrates the importance of incongruent dissolution-precipitation during metasomatism.

Funding

This research did not receive any specific grant from funding agencies in the public, commercial, or not-for-profit sectors.

Declaration of Competing Interest

The authors have no competing interests to declare that are relevant to the content of this article.

Acknowledgement

This work has been supported by the Geological Survey of Norway and Department of Earth and Environmental Sciences, Ludwig-Maximilians-University Munich, Germany. Scanning electron microscopy has been run at the LEO 1450 VP instrument at the Geological Survey of Norway (NGU), at a Hitachi SU5000 at Ludwig-Maximilians-Universität München, Germany, and mineral chemistry analysed by Cameca SX100 electron microprobe at the Institute of Geosciences, University of Oslo. We thank two anonymous referees for helpful comments.

References

Austrheim, H., 1987. Eclogitization of the lower crustal granulites by fluid migration through shear zones. Earth Planet. Sci. Lett. 81, 221–232.
Austrheim, H., Putnis, C., Engvik, A.K., Putnis, A., 2008. Zircon coronas around Fe-Ti oxides: a physical reference frame for metamorphic and metasomatic reactions. Contrib. Mineral. Petrol. 156, 517–527.
Austrheim, H., Engvik, A.K., Ganerød, M., Dunkel, K.G., Roen Velo, M., 2022. Low-grade prehnite-pumpellyite facies metamorphism and metasomatism in basement rocks adjacent to the Permian Oslo rift; the importance of displacive reactions. J. Metamorph. Geol. 40, 1467–1492.
Barrow, G., 1912. On the geology of lower Dee-side and the southern Highland Border. Proc. Geol. Assoc. 23, 274–290.
Bast, R., Scherer, E.E., Mezger, K., Austrheim, H., Ludwig, T., Marschall, H.R., Putnis, A., Löwen, K., 2014. Boron isotopes in tourmaline as a tracer of metasomatic processes in the Bamble sector of Southern Norway. Contrib. Mineral. Petrol. 168, 1069.
Bernier, L., Pouliot, G., MacLean, W.H., 1987. Geology and metamorphism of the Montauban North Gold Zone: a metamorphosed Polymetallic Exhalative Deposit, Grenville Province, Quebec. Econ. Geol. 82, 2076–2090.
Bingen, B., Davis, W.J., Hamilton, M.A., Stein, H.J., Engvik, A.K., Skår, Ø., Nordgulen, Ø., 2008. Geochronology of high-grade metamorphism in the Sveconorwegian belt, S Norway: U-Pb, Th-Pb and Re-Os data. Nor. J. Geol. 88, 13–42.
Brøgger, W.C., 1934. On several Archean rocks from the south coast of Norway. I. Nodular Granites from the environs of Kragerø. Det Norske Videnskaps-Akademi i Oslo Skrifter. Matematisk-Naturvidenskapelig Klasse 8, 97.
Brøgger, W.C., Reusch, H.H., 1875. Vorkommen des Apatit in Norwegen. Z. Dtsch. Geol. Ges. 27, 646–702.
Bugge, J.A.W., 1943. Geological and petrographical investigations in the Kongberg-Bamble formation. Nor. Geol. Unders. 160, 1–150.
Clark, C., Schmidt Mumm, A., Faure, K., 2005. Timing and nature of fluid flow and alteration during Mesoproterozoic shear zone formation, Olary Domain, South Australia. J. Metamorph. Geol. 23, 147–164.
Dahlgren, S., Bogoch, R., Magaritz, M., Michard, A., 1993. Hydrothermal dolomite marbles associated with charnockite magmatism in the Proterozoic Bamble Shear Belt, South Norway. Contrib. Mineral. Petrol. 113, 394–409.
Elliot, R.B., Morton, R.D., 1965. The nodular metamorphic rocks from the environs of Kragerø, south coast of Norway. Nor. J. Geol. 45, 1–23.
Engvik, A.K., Austrheim, H., 2010. Formation of sapphirine and corundum in scapolitised and Mg metasomatised gabbro. Terra Nova 22, 166–171.
Engvik, A.K., Austrheim, H., Andersen, T.B., 2000. Structural, mineralogical and petrophysical effects on deep crustal rocks of fluid-limited polymetamorphism, Western Gneiss Region, Norway. J. Geol. Soc. Lond. 157, 121–134.
Engvik, A.K., Bertram, A., Kalthoff, J., Stöckhert, B., Austrheim, H., Elvevold, S., 2005. Magma-driven hydraulic fracturing and infiltration of fluids into the damaged host rock, an example from Dronning Maud Land, Antarctica. J. Struct. Geol. 27, 839–854.
Engvik, A.K., Putnis, A., FitzGerald, J., Austrheim, H., 2008. Albitization of granitic rocks: the mechanism of replacement of oligoclase by albite. Can. Mineral. 46, 1401–1415.
Engvik, A.K., Golla-Schindler, U., Berndt, J., Austrheim, H., Putnis, A., 2009. Intragranular replacement of chlorapatite by hydroxy-fluor-apatite during metasomatism. Lithos 112, 236–246.
Engvik, A.K., Mezger, K., Wortelkamp, S., Bast, R., Corfu, F., Korneliussen, A., Ihlen, P., Bingen, B., Austrheim, H., 2011. Metasomatism of gabbro – mineral replacement and element mobilization during the Sveconorwegian metamorphic event. J. Metamorph. Geol. 29, 399–423.
Engvik, A.K., Ihlen, P.M., Austrheim, H., 2014. Characterisation of Na-metasomatism in the Sveconorwegian Bamble Sector of South Norway. Geosci. Front. 5, 659–672.
Engvik, A.K., Bingen, B., Solli, A., 2016. Localized occurrences of granulite: P-T modeling, U-Pb geochronology and distribution of early-Sveconorwegian high-grade metamorphism in Bamble, South Norway. Lithos 240-243, 84–103.
Engvik, A.K., Corfu, F., Solli, A., Austrheim, H., 2017. Sequence and timing of mineral replacement reactions during albitisation in the high-grade Bamble lithotectonic domain, S-Norway. Precambrian Res. 291, 1–16.
Engvik, A.K., Taubald, S., Solli, A., Grenne, T., Austrheim, H., 2018. Dynamic metasomatism – stable isotopes, fluid evolution and deformation of albitite and scapolite metagabbro (Bamble lithotectonic domain, South Norway). Geofluids 9325809. https://doi.org/10.1155/2018/9325809.
Engvik, A.K., Mertens, C., Trepmann, C.A., 2020. Episodic deformation and reactions in mylonitic high-grade metamorphic granulites from Dronning Maud Land, Antarctica. J. Struct. Geol. 141, 104196 https://doi.org/10.1016/j.jsg.2020.104196.
Ettner, D.C., Bjørlykke, A., Andersen, T., 1993. Fluid evolution and Au-Cu genesis along a shear zone: a regional fluid inclusion study of shear zone-hosted alteration and gold and copper mineralization in the Kautokeino greenstone belt. Finnmark, Norway. J. Geochem. Explor. 49, 233–267.
Fagereng, A., Diener, J.F.A., Meneghini, F., Harris, C., Kvadsheim, A., 2018. Quartz vein formation by local dehydration embrittlement along the deep, tremorgenic subduction thrust interface. Geology 46, 67–70.
Fitz Gerald, J.D., Stünitz, H., 1993. Deformation of granitoids at low metamorphic grade. I: reactions and grain size reduction. Tectonophysics 221, 269–297.
Frost, B.R., Arculus, R.J., Barnes, C.G., Collins, W.J., Ellis, D.J., Frost, C.D., 2001. A geochemical classification of granitic rocks. J. Petrol. 42, 2033–2048.
Gillen, C., 1982. Metamorphic Geology. George Allen & Unwin, London.
Harlov, D.E., Förster, H.-J., Nijland, T.G., 2002. Fluid-induced nucleation of (Y+REE)-phosphate minerals within apatite: Nature and experiment. Part I. Chlorapatite. Am. Mineral. 87, 245–261.
Hunter, R.A., Andronicos, C.L., 2013. Deformation assisted phase transformation: an example from the sillimanite-in isograd, Eolus batholith, Needle Mountains, Colorado, USA. Terra Nova 25, 48–56.
Jamtveit, B., Austrheim, H., Putnis, A., 2016. Disequilibrium metamorphism of stressed lithosphere. Earth-Sci. Rev. 154, 1–13.
Kihle, J., Harlov, D.E., Frigaard, Ø., Jamtveit, B., 2010. Epitaxial quartz inclusions in corundum from a sapphirine-garnet boudin, Bamble Sector, SE Norway: SiO_2-Al_2O_3 miscibility at high P-T dry granulite facies conditions. J. Metamorph. Geol. 28, 769–784, 10.111/j.1525-1314.2010.00891.x.
Kusebauch, C., John, T., Barnes, J.D., Klügel, A., Austrheim, H.O., 2015a. Halogen Element and Stable Chlorine Isotope Fractionation Caused by Fluid–Rock Interaction (Bamble Sector, SE Norway). J. Petrol. 56, 299–324.
Kusebauch, C., John, T., Whitehouse, M.J., Engvik, A.K., 2015b. Apatite as probe for the halogen composition of metamorphic fluids (Bamble Sector, SE Norway). Contrib. Mineral. Petrol. 170, 34.
Liebscher, A., 2007. Experimental studies in model fluid systems. In: Liebscher, A., Heinrich, C.A. (Eds.), Fluid-Fluid Interactions, Reveiws in Mineralogy and Geochemistry, vol. 65, pp. 15–48.
Lieftink, D.J., Nijland, T.G., Maijer, C., 1994. The behavior of rare-earth elements in high-temperature Cl-bearing aquous fluids: results from the Ødegården Verk natural laboratory. Can. Mineral. 32, 149–158.
Luan, F.C., Paterson, M.S., 1992. Preparation and deformation of synthetic aggregates of quartz. J. Geophys. Res. 97, 301–320. https://doi.org/10.1029/91JB01748.
Maniar, P.D., Piccoli, P.M., 1989. Tectonic discrimination of granitoids. Geol. Soc. Am. Bull. 101, 635–643.
Mark, G., Foster, D.R.W., 2000. Magmatic albite-actinolite-apatite-rich rocks from the Cloncurry district, Northwest Queensland, Australia. Lithos 51, 223–245.
McLelland, J., Morrison, J., Selleck, B., Cunningham, B., Olson, C., Schmidt, K., 2002a. Hydrothermal alteration of late- to post-tectonic Lyon Muntain granitic Gneiss, Adirondack Mountains, New York: Origin of quartz-sillimanite segregations, quartz-albite lithologies, and associated Kiruna-type low-Ti Fe-oxide deposits. J. Metamorph. Geol. 20, 175–190.
McLelland, J., Goldstein, A., Cunningham, B., Olson, C., Orrell, S., 2002b. Structural evolution of a quartz-sillimanite vein and nodule complex in a late- to post-tectonic leucogranite, Western Adirondack Highlands, New York. J. Struct. Geol. 24, 1157–1170.
Mukai, H., Austrheim, H., Putnis, C.V., Putnis, A., 2014. Textural evolution of plagioclase feldspar across a shear zone: implication for deformation mechanism and rock strength. J. Petrol. 55, 1457–1477.

Munz, I.A., Wayne, D., Austrheim, H., 1994. Retrograde fluid infiltration in the high-grade Modum complex, South Norway; evidence for age, source and REE mobility. Contrib. Mineral. Petrol. 116, 32–46.
Nabelek, P.I., 1997. Quartz-sillimanite leucosomes in hig grade schist, Black Hills, South Dakota: a perspective on the mobility of aluminium in high grade metamorphic rocks. Geology 25, 995–998.
Nijland, T.G., Jansen, B.H., Maijer, C., 1993. Halogen geochemistry of fluid during amphibolite–granulite metamorphism as indicated by apatite and hydrous silicates in basic rocks from the Bamble Sector, South Norway. Lithos 30, 167–189.
Nijland, T.G., Harlov, D.E., Andersen, T., 2014. The Bamble Sector, South Norway: a review. Geosci. Front. 5, 635–658.
Oliver, N.H.S., Rawling, T.J., Cartwright, I., Pearson, P.J., 1994. High-temperature fluid-rock interaction and scapolitization in an extension-related hydrothermal system, Mary Kathleen, Australia. J. Petrol. 35, 1455–1491.
Oliver, N.H.S., Cleverley, J.S., Mark, G., Pollard, P.J., Bin, F., Marshall, L.J., Rubenach, M.J., Williams, P.J., Baker, T., 2004. Modelling the role of sodic alteration in the genesis of iron oxide-copper-gold deposits, eastern Mount Isa block, Australia. Econ. Geol. 99, 1145–1176.
Padget, P., Brekke, H., 1996. Geologisk kart over Norge, berggrunnskart Arendal - 1:250 000. Norges geologiske Undersøkelse, Trondheim.
Pouchou, J.P., Pichoir, F., 1984. Cameca PAP program. La Recherch. Aerospat. 3, 167–192.
Putnis, A., 2002. Mineral replacement reactions: from macroscopic observations to microscopic mechanisms. Mineral. Mag. 66, 689–708.
Putnis, A., 2021. Fluid-Mineral Interactions: Controlling coupled Mechanisms of Reaction, Mass transfer and Deformation. J. Petrol. 62, 1–27.
Putnis, A., Austrheim, H., 2010. Fluid-induced processes: Metasomatism and Metamorphism. Geofluids 10, 254–269.
Robie, R.A., Bethke, P.M., 1962. Molar volumes and densities of minerals. In: United States Department of the Interior Geological Survey, Report TEI-822.
Saunders, C.M., Tuach, J., 1988. K-feldspathization, albitization and gold mineralization in granitoid rocks; the Rattling Brook alteration system western White Bay, Newfoundland. Curr. Res. – Mineral Develop. Divis. (St. Johns) 88, 307–317.
Spry, P.G., Mcfadden, S., Teale, G.S., Alers, B., Shalloe, J.M., Glenn, J.M., 2022. Nodular sillimanite rocks as field indicators to metamorphosed massive sulphide deposits. Ore Geol. Rev. https://doi.org/10.1016/j.oregeorev.2021.104632.
Stöckhert, B., Brix, M.R., Kleinschrodt, R., Hurford, A.J., Wirth, R., 1999. Thermochronometry and microstructures of quartz – a comparison with experimental flow laws and predictions on the temperature of the brittle-plastic transition. J. Struct. Geol. 21, 351–369.
Tokle, L., Hirth, G., Behr, W.M., 2019. Flow laws and fabric transitions in wet quartzite. Earth and Plant. Sci. Lett. 505, 152–161.
Touret, J.L.R., 1971. Le faciès granulite en Norvège méridionale. I Les associations minéralogiques. Lithos 4, 239–249.
Vernon, R.H., 1979. Formation of late sillimanite by hydrogene metasomatism (base leaching) in some high-grade gneisses. Lithos 12, 143–145.
Wassmann, S., Stöckhert, B., 2013. Rheology of the plate interface – dissolution precipitation creep in high pressure metamorphic rocks. Tectonophysics 608, 1–29.
Wassmann, S., Stöckhert, B., Trepmann, C.A., 2011. Dissolution precipitation creep versus crystalline plasticity in high-pressure metamorphic serpentinites. In: Prior, D. J., Rutter, E.H., Tatham, D.J. (Eds.), Deformation Mechanisms, Rheology and Tectonics: Microstructures, Mechanics and Anisotropy, vol. 360. Geological Society London Special Publications, pp. 129–149.
Wayte, G.J., Worden, R.H., Rubie, D.C., Droop, G.T.R., 1989. A TEM study of disequilibrium plagioclase breakdown at high pressure: the role of infiltrating fluid. Contrib. Mineral. Petrol. 101, 426–437.
Weisheit, A., Bons, P.D., Elburg, M.A., 2013. Long-lived crustal-scale fluid flow: the hydrothermal mega-breccia of Hidden Valley, Mt. Painter Inlier. South Australia. Int. J. Earth Sci. 102, 1219–1236.
Wheeler, J., 1992. Importance of pressure solution and coble creep in deformation of polymineralic rocks. J. Geophys. Res. 97, 4579–4586.
Whitney, D.L., Evans, B.W., 2010. Abbreviations for names of rock-forming minerals. Am. Mineral. 95, 185–187.
Wintsch, R.P., Yi, K., 2002. Dissolution and replacement creep: a significant deformation mechanism in mid-crustal rocks. J. Struct. Geol. 24, 1179–1193.
Wintsch, R.P., Aleinikoff, J.N., Yi, K., 2005. Foliation development and reaction softening by dissolution and precipitation in the transformation of granodiorite to orthogneiss, Glastonbury complex, Connecticut, USA. Can. Mineral. 43, 327–347.